Energy Equip. Sys./ Vol. 5/No.4/December 2017/ 401-409

ENERGY EQUIPSYS

Energy Equipment and Systems

http://energyequipsys.ut.ac.ir
www.energyequipsys.com

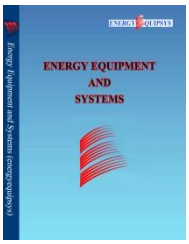

The finite element analysis of the linear hybrid reluctance motor for the electromagnetic launch system

Authors

Hassan Moradi Cheshmehbeigi [a]*
Farzad Fathinia [a]

[a] Electrical Engineering Department, Engineering Faculty, Razi University, Kermanshah, Iran

Article history:

Received : 7 November 2016
Accepted : 8 April 2017

ABSTRACT

The Electromagnetic Aircraft Launch System (EMALS) is being developed utilizing electrical and electronic technologies. EMALS is emerging in order to replace the existing steam catapult on naval carriers. Recently, the double-sided linear launcher has drawn increasing attention of researchers. This paper presents the design and analysis of the Linear Hybrid Reluctance Motor (LHRM). This new motor is characterized by a stator, formed by a combination of independent magnetic structures. Each magnetic structure is composed of an electromagnet—the magnetic core with one or several coils wound around it and associated with a permanent magnet, disposed between their poles. The rotor has the same configuration of a switched reluctance motor (SRM) without any coil, magnets or squirrel cage. In order to improve the thrust of LHRM, the structural characteristics and magnetic field are analyzed. According to the initial design, the Finite Element Analysis (FEA) is presented to obtain the magnetic cogging force and thrust force. Moreover, the effects of the parameters on the thrust and thrust ripple waveforms are analyzed using FEA.

Keywords: EMALS, LHRM, Double-Sided, FEA, Magnetic Field Analysis.

1. Introduction

The Electromagnetic Aircraft Launch System (EMALS) is the next generation aircraft launching system of the US Navy for 21st century aircraft carriers. EMALS will greatly enhance the operational capabilities of the carriers. It does so by expanding the performance envelope over the current launch system to handle aircrafts at a much wider range of launch speeds and energies. As pointed out by Richard R. B. (2001), this new launch system will be more efficient, controllable, and will reduce the weight, volume, and total ownership cost from the current steam catapult system. One of EMALS's most important benefits to the ship is that it imparts increased flexibility to the layout of the launch system components. This allows greater optimization of the ship's internal arrangement, including better load distribution. The elimination of steam dependence allows a more optimal and efficient ship power plant design. In essence, EMALS opens up the trade space for both naval

* Corresponding author: Hassan Moradi Cheshmehbeigi
Address: Electrical Engineering Department, Engineering Faculty, Razi University, Kermanshah, Iran
E-mail address: ha.moradi@razi.ac.ir

architects and aeronautical engineers in designing the future navy as presented by M.R. Doyle et al. (1995). EMALS is a complete launch system designed to replace the existing steam catapult. The basic design consists of energy storage/ power generation subsystem, a power conditioning subsystem, a launch motor, and a control system. The approach in Patterson D. et al. (2005) shows these subsystems combining to provide a highly capable launch system. This launch system expands the operational capability of future carriers to allow for heavier and faster aircraft. In addition, it permits the operation of small and lightweight air vehicles that are currently not compatible with the steam catapult. This paper has further discussed the linear motor part of EMALS. The linear motor for electromagnetic launch generally requires high voltage, high current, and high and constant thrust. The variation range of transient velocity for the mover is very large. Moreover, the terminal velocity can reach several tens meters per second, as presented by Kou B. Q. et al. (2009). All these special conditions require high thrust output and energy efficiency for Linear Hybrid Reluctance motor (LHRM). Therefore, the study of structural parameters and electrical parameters effected rule are necessary to promote the performance of LHRM design. In recent years, Switched Reluctance Motor (SRM) has been proven to provide the best overall performance for EMALS applications as compared to other electric motors. This is because of the high torque/ inertia ratio and efficiency, low manufacturing and operating costs, and fault tolerance of EMALS, as presented by Hao C. and Qianlong W. (2013). The double-sided plate SRM has received increasing attention in the industry. As pointed out by Mahir D. and Harun Ö. (2011), the two-sided normal forces in the double-sided plate motor counteract each other. The basic structure of a double-sided LHRM is shown in Fig. 1.

2. Proposed linear hybrid reluctance motors

This paper presents a new type of LHRM, which is characterized by a stator. The stator here is formed by the combination of independent magnetic structures, composed of an electromagnet. An electromagnet is defined as a type of magnet comprising of a magnetic

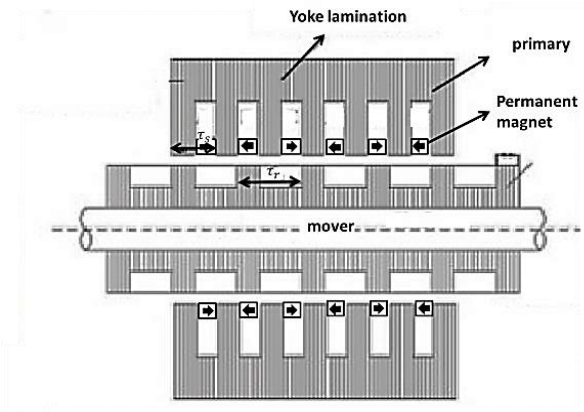

Fig. 1. Basic structure of a double-sided LHRM

core with one or several coils wound around it and associated with a permanent magnet disposed between their poles. As presented by P. Andrada et al. (2012), the rotor has the same configuration as that of an SRM without any coil, magnets, and squirrel cage as such. The motor is controlled by an electronic power converter, in which the switching sequence of the phases is generated according to the rotor position. This position, as pointed out by Hao Ch. et al. (2013), is determined by a speed–position transducer or estimated by means of the voltages and currents of the motor.

Figure 2(a) shows the magnetic circuit of an electromagnet—consisting of a fixed part (U shaped), with a coil of N turns, and a movable part. These parts are built using ferromagnetic materials (laminated electrical steel, soft magnetic composites, etc.), separated by an air gap. When current flows through the coil, a magnetic field is created, which in turn produces an electromagnetic force. The electromagnetic force attracts the moving part once the forces opposing to the movement have been overcome. Figure 1(b) shows the same magnetic circuit that is shown in Fig. 2(a). Unlike Fig.2(a), Fig.1(b) shows a permanent magnet placed near the air gap, inside the fixed part (U shaped) of the electromagnet. When no current flows through the coil, the flux created by the magnet is closed through the fixed part and does not cross the air gap, as is seen in Fig. 2(b). However, when current flows through the coil, the flux of the magnet is added to the flux generated by the action of the coil (see Fig. 2[c]). This creates an electromagnetic attraction force superior to that produced by a conventional electromagnet.

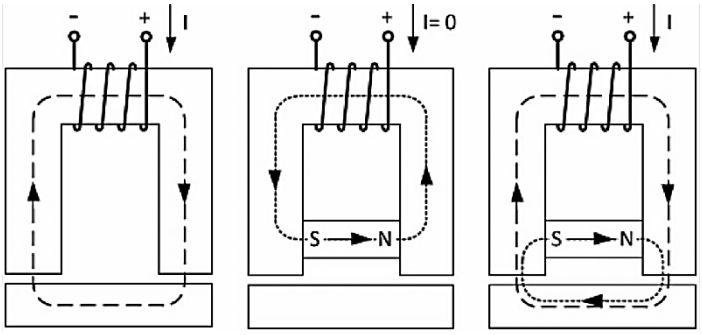

Fig. 2. (a). Flux distribution in an electromagnet with current passing through the coil; (b). Flux distribution in an electromagnet with permanent magnet without passing current through the coil; (c). Flux distribution in an electromagnet with permanent magnet with current passing through the coil.

3. Force production in linear hybrid reluctance motors

In the Linear Hybrid Reluctance Motor (LHRM), the main force component is generated due to the variation in the reluctance. To better describe the design parameters that affect force production in the LHRM, the principle of force production was briefly described first by T. J. E. Miller (1985). The energy transferred to the magnetic system (W_e) may be described as:

$$\begin{cases} W_e = W_{supply} - \Delta W_{cu} \\ = \int \left(u.i - R.i^2\right) dt \\ = \int id\Psi\left(l,i\right) \end{cases} \quad (1)$$

where W_{supply} is the energy from the supply, l is the motor length, and W_{cu} is the copper loss. Ignoring iron losses, the field energy $\left(W_{field}(\Psi,l)\right)$ is presented as:

$$W_{field}\left(\Psi,l\right) = W_e\left(l,i\right) - W_{em}\left(l\right) - W_{cog}\left(l\right) \quad (2)$$

W_{em} is the energy delivered to the mechanical subsystem of the machine from the magnetic subsystem. W_{cog} is the energy stored in the magnets. By changing the load of the magnet (i.e., by varying the air-gap), the stored energy of the magnet will change. This gives rise to cogging force (permanent magnet reluctance force).

Based on the difference between the flux linkage and the current curves (shown in Fig. 3) at the minimum and maximum inductance positions (known as aligned and unaligned positions, respectively), the calculation of the average reluctance force may be carried out as:

$$\begin{cases} \Delta W_{em} = \Delta W_e - \Delta W_{field} \\ \Delta W_{em} = Area_{OAB} \end{cases} \quad (3)$$

$$F_{av} = \frac{mN_P}{l} \Delta W_{em} \quad (4)$$

Where m is the number of phases and N_P is the number of rotor poles.

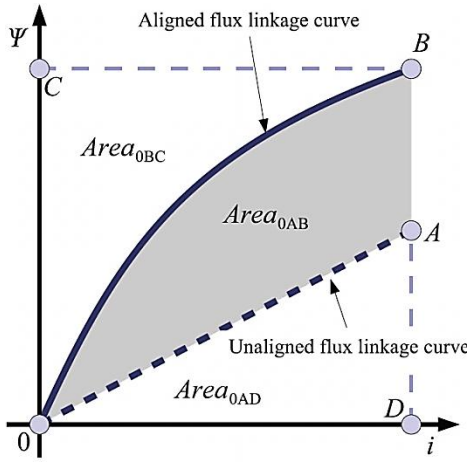

Fig. 3. Determination of the electromagnetic torque for an LHRM

The electromagnetic torque for LHRM is calculated based on Fig. 4. For LHRM, with permanent magnet field present at the unaligned position, the flux linkage vs. current curve at the unaligned position will then have an offset flux linkage value at zero current. This is shown in Fig. 4. Similarly, the average force may be calculated as:

$$\begin{cases} \Delta W_{em} = \Delta W_e - \Delta W_{field} \\ \Delta W_{em} = Area_{DABC} \end{cases} \quad (5)$$

$$F_{av} = \frac{mN_P}{l}\Delta W_{em} \quad (6)$$

Where the energy associated with the cogging force (W_{cog},) is not involved, as the average cogging force value is always zero. As it may be observed from Fig. 4, with permanent magnet flux present, the unaligned flux-linkage-current curve has been moved towards the negative direction of the flux linkage axis. The aligned curve is also shifted downwards, but not as much as the unaligned curve. The total enclosed area by these two flux-linkage-current curves, denoted as Area DABC, is equivalent to the energy used for force production, which has increased due to the additional permanent magnet field.

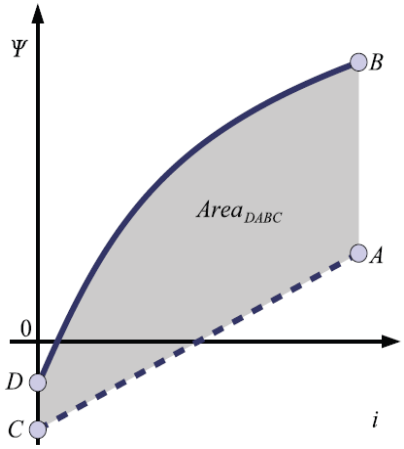

Fig. 4. Determination of the electromagnetic torque for LHRM. Notice that both the unaligned and aligned flux linkage may not start at zero due to flux from the permanent magnets.

4. Optimization

One of the most important drawbacks of LHRM is the thrust ripple. Therefore, one of the objective functions of this paper is its minimization. Another important subject in LHRM is the maximization of the average thrust. A multi-objective optimization is discussed and both thrust ripple and thrust density are improved. The constraints are maximum flux density in teeth (*Bmax)* and maximum current flow (*imax).* The parameters affecting force ripple and thrust force are selected as design variables and the other parameters are selected as fixed variables. The design variables and the range values are listed in Table 1A schematic model established under one pole pitch, as shown in Fig. 5.

Table 1. Nominal value of the geometrical parameters of the LHRM

	Symbol	Range Value	Unit
Magnet thickness	h_M	11–14	mm
Coil diameter	d_c	8–11	mm
Slot depth	d_s	18–21	mm
Slot width	w_s	40–55	mm

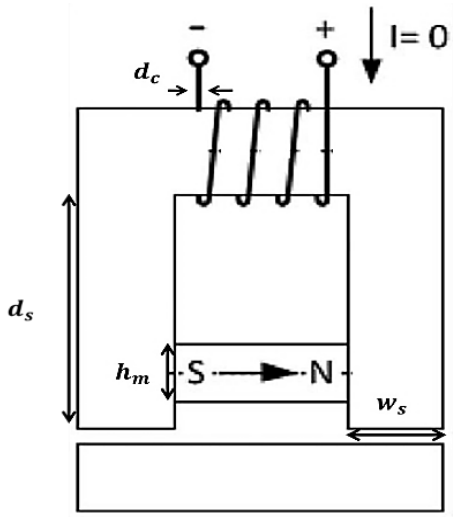

Fig. 5. Schematic model of thrust density under one pole pitch

The parametric search is used for multi-objective optimization of LHRM. The methods are made in a 2D FEA software for the displacement of the translator with a polar step and with 10 Time Step (TS) of the simulation. The chosen values of TS are: 1/10τs, 1/5τs, 3/10τs, 2/5τs, 1/2τs, 3/5τs, 7/10τs, 4/5τs, 9/10τs, and τs. The thrust and ripple for each step of time are a mean value of the data obtained for simulation with the displacement of a polar, which is enumerated as:

$$J_{Ts}^{c} = k_1 * \left(max\left\{ \left| F_{ripple}\left(Ts_0\right) \right| \right\} \right)^2 + k_2 * \frac{1}{\left(F_{thrust}\left(Ts_0\right) \right)^2} \quad for \quad 0 \le Ts_0 \le \tau s \quad (7) \quad (7)$$

where k_1 and k_2 are weight functions. In the studied case, an equal weight of one is given to both the functions as the maximization of amplitudes of thrust is as important as thrust ripple diminishing. Here, c is the range value of parameters and the step of value change with *ic* is also shown. A flowchart of the FEA is shown in Fig. 6.

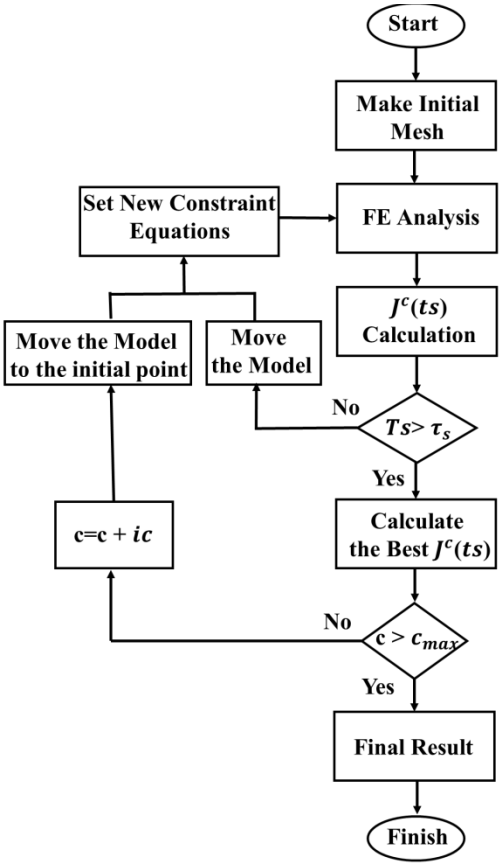

Fig. 6. A flowchart of the FEA

5. Finite-element analysis of lhrm

As shown in Fig. 1, the finite element analysis model of the moving-magnet-type LHRM is established. Fig. 7 shows the meshed model of LHRM by FEA. It can be seen that the magnets, drive coil, and tooth are relatively intensive, so as to ensure the accuracy of simulation.

The magnetic-flux-line for LHRM is shown in Fig. 8. It can be seen that the magnetic circuit structure is complex, uniform, and with low flux leakage. It is important to note that the flux of the magnet in the nonexcited phases closes through the yoke and does not cross the air gap.

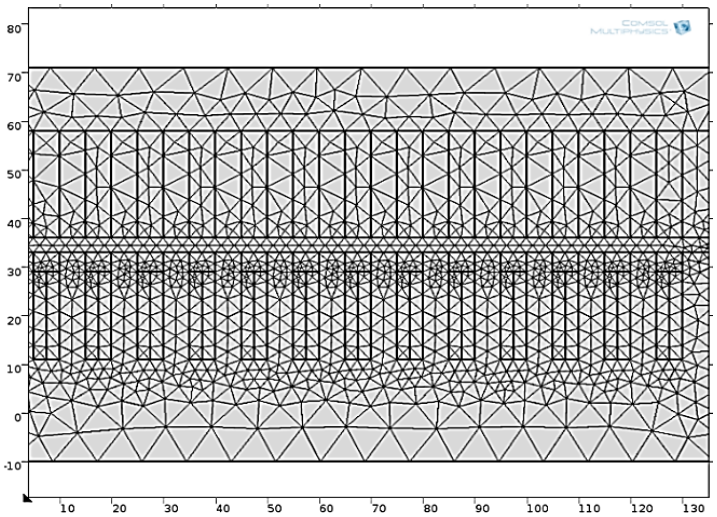

Fig. 7. The triangular meshed model of LHRM by FEA

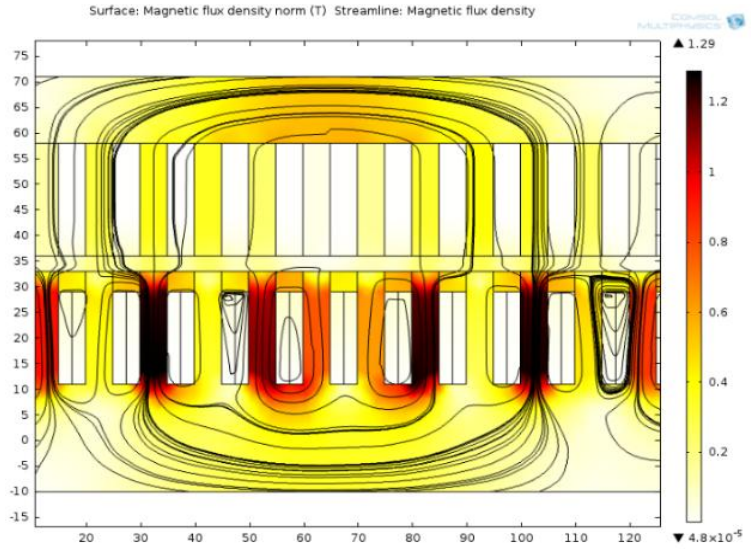

Fig. 8. The flux linkage distribution for LHRM

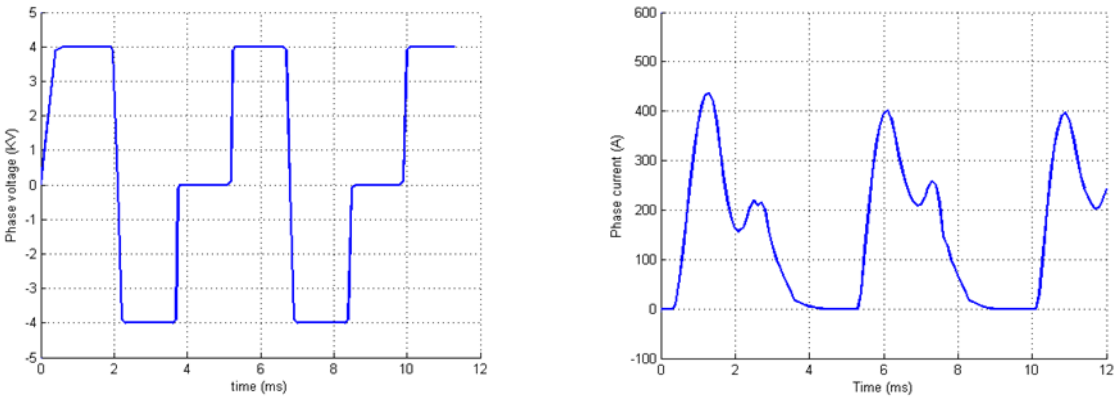

(a) (b)

Fig. 9. The phase voltage and current waveform: (a) phase voltage waveform (b) phase current waveform

The waveforms of the phase voltage control are shown in Fig. 9(a). The waveforms of the phase current are shown in Fig. 9(b). The main advantage of voltage control over current control is that the voltage control typically requires only one current sensor in the dc link for overcurrent protection.

The evolution of the force, due to the interaction between the permanent magnets and the rotor poles, versus position—when there is no current in the coils—is shown in Fig. 10. This force is usually called cogging force or detent force and is an undesirable effect in the operation of the motor. The results derived from Fig. 10 confirm that cogging force is virtually zero in this new hybrid motor. This is because there are no flux lines that cross the air gap when there is no circulation of current by the coils. This is a clear advantage of the present LHRM over other types of LHRM.

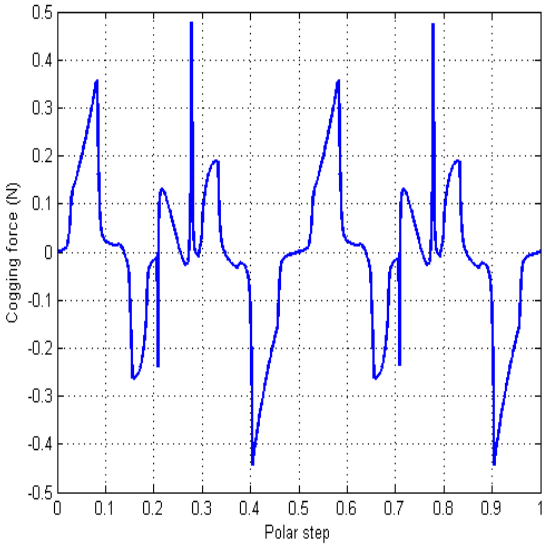

Fig. 10. Cogging force versus position (without current in the coils)

Figures 11 and 12 show the thrust and the thrust ripple results under different thickness of the PM, respectively. The results indicate that the thrust increases as the thickness of the PM varies—the maximum thrust of LHRM is 12530N for a thickness of PM=14mm, and the thrust ripple ratio reaches the minimum at 12mm. By considering the thrust ripple ratio and ripple the optimum value for PM thickness = 13 mm.

The impact analysis of the coil diameter is very important for estimating the actual performance. The responses of the thrust and the thrust ripple ratio with different coil diameters are shown in Figs. 13 and 14, respectively. The thrust is increased according to the increase in coil diameter. However, the coil diameter is limited by the current constraint. These variables have the optimum value of minimizing the thrust ripple and maximizing the thrust force.

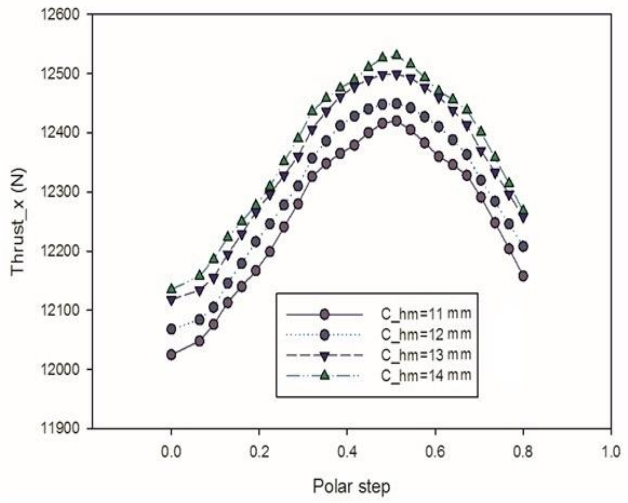

Fig. 11. Result of Thrust based on step of time (TS) considering thickness of the PM

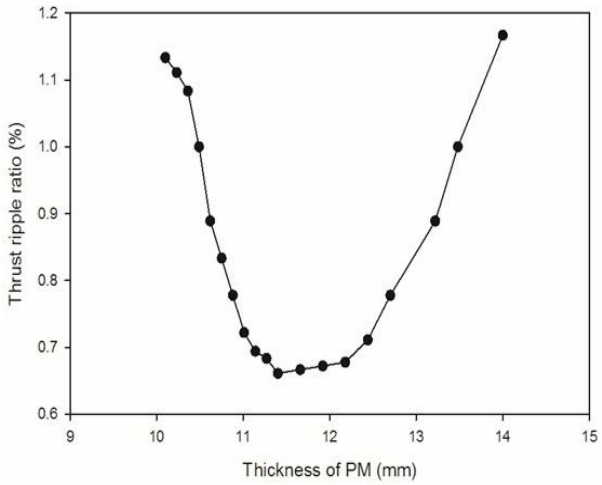

Fig. 12. Thrust ripple ratio with different thickness of PM

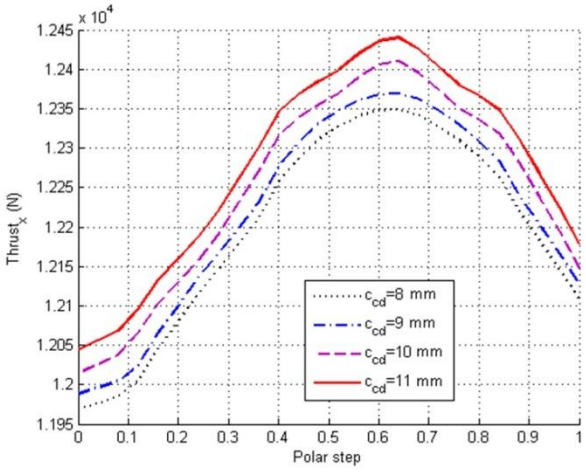

Fig. 13. Result of Thrust based on step of time (TS) considering coil diameter c_{cd}

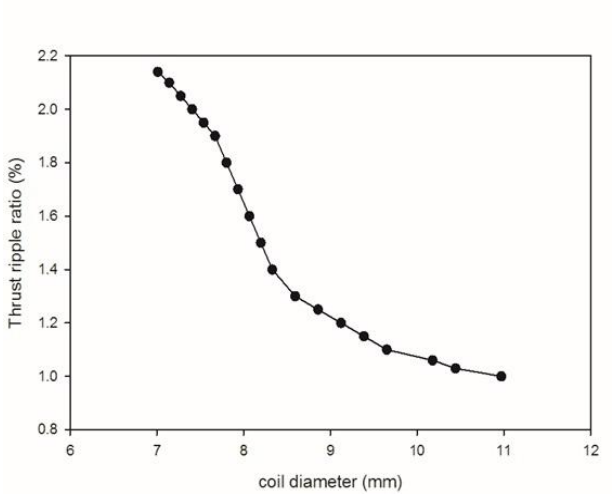

Fig. 14. Thrust ripple ratio with different coil diameter (c_{cd})

Figures 15 and 16 are shown thrust and the thrust ripple results under different slot depth (c_{ds}), respectively. The acquired results show that the increase in thrust as the depth of the groove is different, But rate slows down and tends to saturation, the amplitudes of thrust of LHRM as follow the higher amplitude obtained for the slot depth =24 mm. But the minimum thrust ripple ratio of LHRM are 1.9% for the slot depth =18 mm. By considering the thrust ripple ratio and ripple the optimum value for slot depth= 22 mm.

Figures 17 and 18 show the thrust and the thrust ripple results under different width of slot (c_{ws}), respectively. The thrust due to increase of width of slot is increased, but the gap is limited flux density limits, the amplitudes of thrust of LHRM as follow the higher amplitude obtained for the width of slot =50 mm. The thrust ripple ratio of LHRM is 1.94% for the width of slot =50 mm.

Table 2 lists the values of optimized design variables and fixed variables. It also lists the characteristic values of the linear LHRM, calculated using the nominal and optimized design variables. By optimizing the design, the normalized force ripple is reduced to 8.7% and the thrust force is increased to 12.84N compared to the ones not using design optimization.

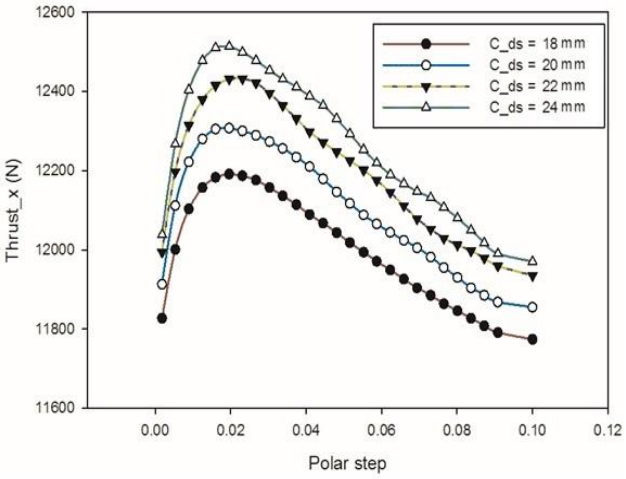

Fig. 15. Result of Thrust based on step of time (TS) considering slot depth (c_{ds})

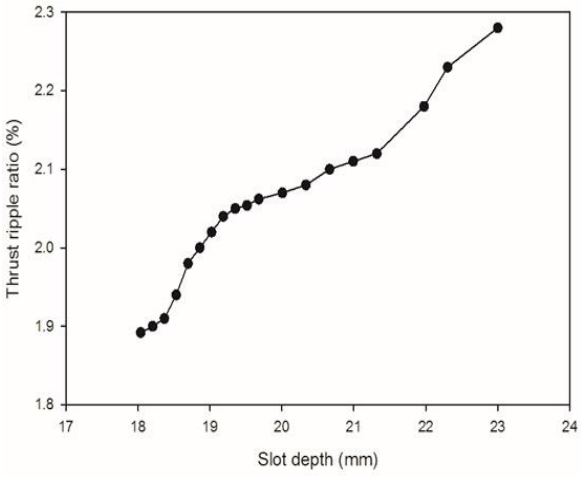

Fig. 16. Thrust ripple ratio with different slot depth

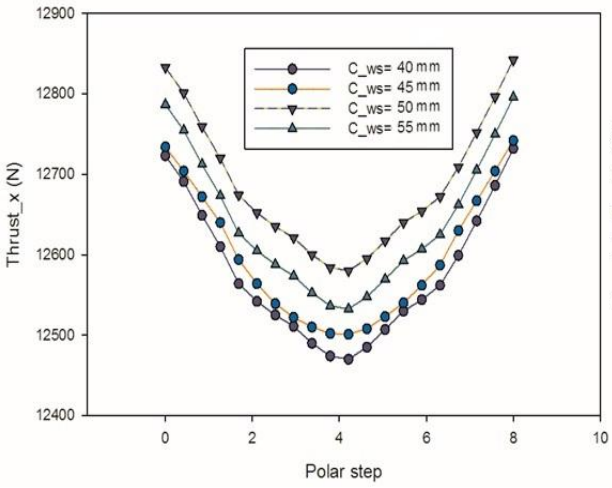

Fig. 17. Result of Thrust based on step of time (TS) considering slot width (c_{ws})

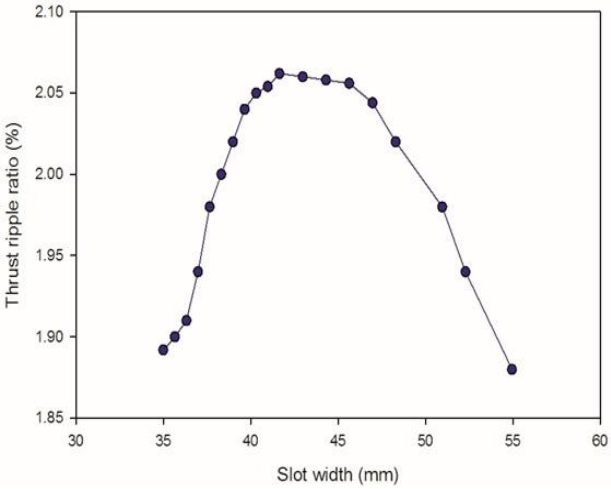

Fig. 18. Thrust ripple ratio with different slot width

Table 2. Optimized design variable and fixed variable

	Symbol	Range Value	Unit
Magnet width	w_M	55	mm
Magnet thickness	h_M	13	mm
Coil diameter	d_s	11	mm
Slot depth	d_c	22	mm
Slot width	w_s	50	mm
Pole pitch	τ	60	mm
Slot pitch	τ_s	10	mm
Residual flux density	B_r	1.2	T
Air gap length	g	3.5	mm
Rated current	I_m	420	A

6. Conclusions

In this paper, a modest attempt has been made to discuss the design of LHRM in EMALS. It uses the PM flux to an advantage. Therefore, this motor has higher force density than conventional switched reluctance motors. Based on the results, this paper establishes the finite element method and analyzes the effects of the parameters on the thrust and thrust ripple performance for EMALS. Many important designs and installation guides can be acquired from this study. The design of LHRM configuration helps in achieving high thrust force. There are no flux lines that cross the air gap when there is no circulation of current by the coils, thereby reducing thrust force ripple.

Reference

[1] Richard R. B., Electromagnetic Aircraft Launch System Development Considerations, IEEE Transactions on Magnetics (2001) 37(1):52–54.

[2] Doyle M.R., Samuel D.J., Conway T., Klimowski R.R, Electromagnetic Aircraft Launch System-EMALS, IEEE Transactions on Magnetics (1995) 31(1): 528 – 533.

[3] Patterson D., Monti A., Brice C.W., Dougal R.A., Pettus R.O., Dhulipala S., Kovuri D.C., Bertoncelli T, Design and Simulation of a Permanent-Magnet Electromagnetic Aircraft Launcher, IEEE Transactions on Magnetics (2005) 41(2) 566 – 575.

[4] Kou B. Q., Huang X.Z., Wu H.X, Li L.Y., Thrust and Thermal Characteristics of Electromagnetic Launcher Based on Permanent Magnet Linear Synchronous Motors, IEEE Transactions on Magnetics, (2009) 45(1):358 – 362.

[5] Hao C., Qianlong W., Modeling of Switched Reluctance Linear Launcher, IEEE Plasma Science (2013) 41(5):1123 – 1130.

[6] Mahir D., Harun Ö., Design and Analysis of a Double Sided Linear Switched Reluctance Motor Driver for Elevator Door, PRZEGLĄD ELEKTROTECHNICZNY (Electrical Review), ISSN 0033-2097(2011).

[7] Andrada P., Blanqué B., Martínez E., Torrent M., New Hybrid Reluctance Motor Drive, in Process ICEM, Marseille, France (2012) 2689–2694.

[8] Hao Ch., Qianlong W., Herbert Ho-Ching I., Acceleration Closed-Loop Control on a Switched Reluctance Linear Launcher', IEEE Plasma Science (2013) 41(5) 1131-1137.

[9] Miller T. J. E., Converter Volt-Ampere Requirements of the Switched Reluctance Motor Drive, IEEE Transactions on Industry Applications (1985) 21 (5): 1136-1144.